Available online at www.eccomasproceedia.org
Eccomas Proceedia COMPDYN (2023) 477-496

ECCOMAS
Proceedia

COMPDYN 2023
9th ECCOMAS Thematic Conference on
Computational Methods in Structural Dynamics and Earthquake Engineering
M. Papadrakakis, M. Fragiadakis (eds.)
Athens, Greece, 12-14 June 2023

DYNAMIC ANALYSIS AND EXPERIMENTAL VERIFICATION OF THE MECHANICAL CHARACTERISTICS OF VARIABLE CROSS-SECTION INDUSTRIAL PYLONS

Konstantinos Katakalos[1], George D. Manolis[2], George C. Manos[2], Lazaros Melidis[3], Georgios Dadoulis[3], Vasil Kavardzikov[4] and Georgi Stoilov[5]

[1]Assistant Professor and Director; [2]Professor Honorarius; [3]PhD Candidate
Laboratory for Experimental Strength of Materials and Structures
Department of Civil Engineering
Aristotle University of Thessaloniki (AUTh), 54124 Thessaloniki, Greece
{kkatakal; gdm; gcmanos; lmelidis: dadoulis}@civil.auth.gr

[4]Professor; [5]Associate Professor
Department of Solid Mechanics, Institute of Mechanics
Bulgarian Academy of Sciences (BAS), 1113 Sofia, Bulgaria
{kavarj; gstoilov}@imbm.bas.bg

Abstract

Variable cross-section pylons are mass produced and commonly used as components in civil engineering infrastructure, e.g., as lighting posts, in electric power lines, as wind turbines, etc. In this work, full-scale, metallic cantilevered pylons with variable cross-section were tested for use as highway lighting posts. The basic testing protocol was for fatigue, which is a low frequency, small amplitude, multiple cycle pushover test using an actuator at the top of the pylon. In terms of recording devices, a linear variable differential transducer was used for measuring displacements. Additionally, a digital imaging correlation technique was used, which gave a complete picture of the displacement field along the front face of the pylon and across the entire height. Finally, an impact hammer test was used to determine the dynamic properties of the pylon, with accelerations measured at three locations along the height of the pylon. These experimentally obtained measurements were supplemented by numerical modelling, starting with a representation of the pylon as a waveguide. This has an advantage in dynamic analyses, since it is possible to reduce the numerical model to one comprising a small number of eigenmodes, usually with as little as two. In parallel, a fully-fledged finite element method model was developed for a more detailed representation of the response of the pylon, including the question of base fixity, using a few hundred degrees-of-freedom. Finally, comparisons were carried out to help interpret the experimentally obtained results and give a complete picture of the mechanical behavior of the industrial pylon, which is useful in refining its design and for subsequent structural health monitoring purposes.

ISSN:2623-3347
Peer-review under responsibility of the organizing committee of COMPDYN 2023.
doi: 10.7712/120123.10415.20741

Keywords: Experimental verification; Continuous systems; Modal analysis; Finite elements; Impact; Digital image processing; Fatigue testing

1 INTRODUCTION

Civil engineering infrastructure is vulnerable to the deterioration and loss of functionality due to structural aging and to the action of external loads [1]. Briefly, critical infrastructure is classified as the necessary networks that support the built environment. This would include electric power grids; wind turbines; oil and gas pipelines; water and sewage pipes; communication antennas; large-scale construction such as bridges, tunnels, etc. Since the purpose of these networks is to serve the needs of society, their operation must remain continuous over time inasmuch as possible. Moreover, in terms of infrastructure resilience, assets with a high risk of exposure need to be effectively maintained so as to quickly recover in the event of natural disasters [2]. Traditionally, maintenance of critical infrastructure has been conducted following non-destructive testing evaluation practices, such as on-site visual inspections. However, inspections that rely on the availability and judgment of skilled personnel inevitably delays the inspection protocol and introduces bias in assessing the structural condition. Advances in sensor technologies during recent decades [3] have enabled the development of the Structural Health Monitoring (SHM) paradigm [4], whereby critical infrastructure networks are continuously monitored for their overall performance and their response to environmentally induced loads is carefully assessed [5]. Data streams generated by continuous monitoring can be processed with the aid of Artificial Intelligence (AI) algorithms [6], [7], which allows the managing authorities to reach rational conclusions regarding network operations and their maintenance based on this information.

A basic component of civil engineering infrastructure are rod and beam elements, with the former comprising trusses and lattices, while the latter are pylons and cantilevers supporting various non-structural attachments [8]. Over time, much work has been reported in the literature on the dynamic response of beam and rod types of structures that are used, among other functions, as the backbone of critical infrastructure networks [9], [10], [11], [12]. In practice, a number of loading scenarios must be considered for the analysis and design of such structural elements, starting with the dead and live design loads and moving to various categories of external forces, including ambient vibrations, wind pressure and ground motions. Given the complexity of the problem, sometimes recourse is made to statistical methods of analysis [13]. As previously mentioned, various non-structural components are attached to the structural elements comprising a network. These components are often modelled as mass attachments that have no role in modifying the structural stiffness but can modify the dynamic response of the supporting structure if the dynamic loads have a frequency content that leads to resonance. As a result, these masses may be considered as passive or even semi-active control devices [14], [15]. In general, it is possible to view a structural element with an attached mass as a system comprising a primary linear oscillator and a secondary system, provided the latter's mass is small in comparison to the mass of the supporting element.

Testing for fatigue is now an integral part for the certification of infrastructure components that are continuously exposed to the elements [16]. Actually, cyclic testing is

closely related to testing for dynamic loads, since the former is basically a quasi-static procedure, i.e., a slowly varying dynamic load [17]. In recent times, this type of testing can be incorporated within the structural health monitoring (SHM) protocol, which is being increasingly applied for gaining insights to the structural condition of civil engineering infrastructure [18]. In order to describe the actual condition of monitored structures through an estimate of key structural parameter values, system identification is frequently employed [19]. Moreover, collecting acceleration response data from oscillating structures is common practice in SHM, so several system identification methods have been developed for interpreting their dynamic characteristics [20]. In this direction, operational modal analysis (OMA) methods have been drawing increasing attention, owing to the relatively low implementation cost and negligible operating interference [21]. In order to extract structural dynamic parameter values, OMA methods are either applied directly either to the raw, transient acceleration response data or to the frequency domain acceleration response data that has been transformed via the fast Fourier transform (FFT). As output, OMA methods yield estimates for structural dynamic properties, such as natural frequencies, mode shapes, and damping ratios.

The aforementioned methods collect data at discrete locations in the components of a structural system. A different class of techniques capable of recording data across the entire structure is based on optics. More specifically, speckle photography that was originally developed in the 1970s [22], has been employed in developing techniques that utilize correlation analysis of images in experimental mechanics, which can successfully reproduce the kinematic fields that develop in a specimen due to action of external loads. The development of digital, high-speed cameras in tandem with advanced computer hardware and software, has greatly accelerated progress and resulted in the development of alternatives to speckle photography, such as a technique known as Digital Image Correlation (DIC) analysis [23]. Nowadays, a DIC setup comprises a light source, a digital camera and a computer with software that implements algorithms for image correlation analysis, resulting in a method that is fast, reliable and practical. More specifically, DIC is a computer-based image analysis technique utilizing random patterns, which finds applications in experimental mechanics involving solids and structures. In the DIC method, two speckle images are compared. The initial (reference) image, labelled as ‘zone of interest’, is divided into subsets, which are square matrices containing pixels. The choice of subsets depends on the region of interest, i.e., the area where the deformation field is sought. A correspondence between each reference subset with its respective calculated subset from the second (deformed) image, is then established by computing the maximum values of the correlation coefficients [24].

In here, we report on the results of a series of experiments conducted on metallic pylons used for highway lighting purposes, namely fatigue testing, impact hammer tests, and DIC for cyclic loads. These results are corroborated by analytical models and by the finite element method (FEM). The aim of this study is ascertain the suitability of these industrial pylons for their specific use, and to set the groundwork for subsequent SHM purposes.

2 INDUSTRIAL PYLON CASE STUDY

Two identical pylons were brought in for testing at the Laboratory for Experimental Strength of Materials and Structures of AUTh, and a typical setup is shown in Fig. 1. These

are metallic, cantilevered beams with tapering, used for supporting lighting equipment for highway illumination. In more detail, Fig. 2 depicts the geometry of the pylon, which is a circular cylinder with a hollow cross-section of a constant thickness d, bolted to the floor with a metallic base plate as the interface. The cross-section mean radius varies with height L, i.e., $r(x), 0 \leq x \leq L$, where $L = b - a$. For small thickness, the cross-section area and the moment of inertia are closely approximated as $A = 2\pi rd,\ I = \pi r^3 d$, while the mass per unit length is $m = \rho A$. If we assume a quadratic variation of the radius with height as $r(x) = r_0(x/a)^2$, where $r_0 = r(a)$ is the radius at the top, then the pylon axial stiffness, flexural stiffness and mass per length are respectively given as $EA(x) = (EA)_0(x/a)^2$, $EI(x) = (EI)_0(x/a)^6,\ m(x) = m_0(x/a)^2$. Subscript zero indicates reference values computed at the top and E is the elasticity modulus. Table 1 lists the mechanical properties of the pylon, as provided by the manufacturer and measured in the Laboratory, while Fig. 3 shows details relevant to the mathematical modelling of the pylon.

Figure 1: Industrial pylon test setup in the AUTh Laboratory for Experimental Strength of Materials & Structures depicting an actuator at the top and the base attachment system

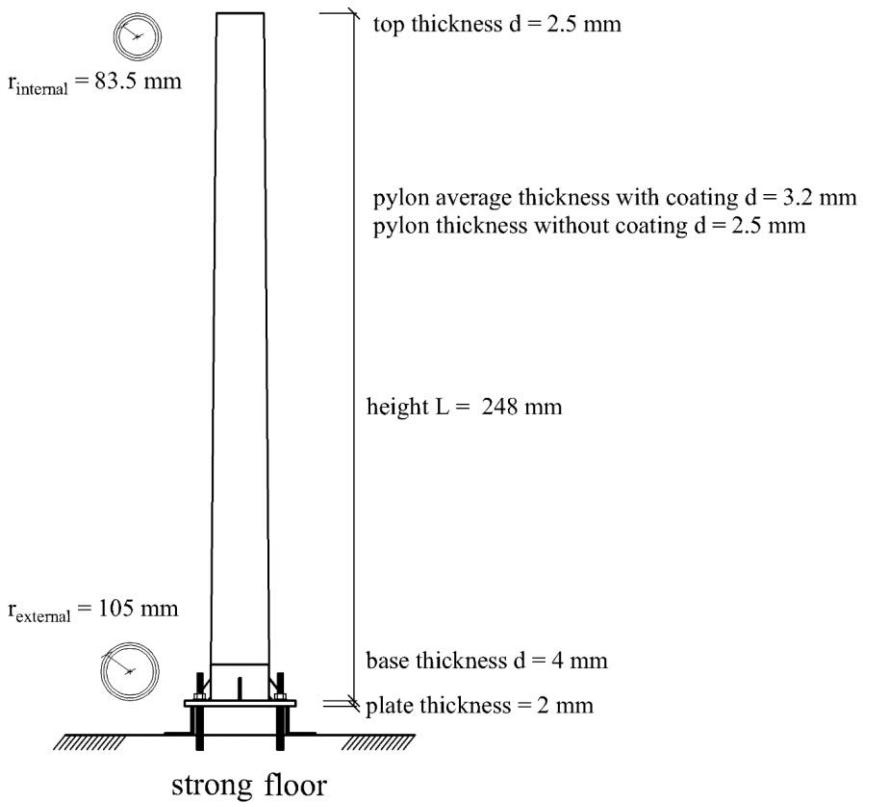

Figure 2: Schematic view of the industrial pylon geometry and of the base attachment to the strong floor of the Laboratory for Experimental Strength of Materials and Structures

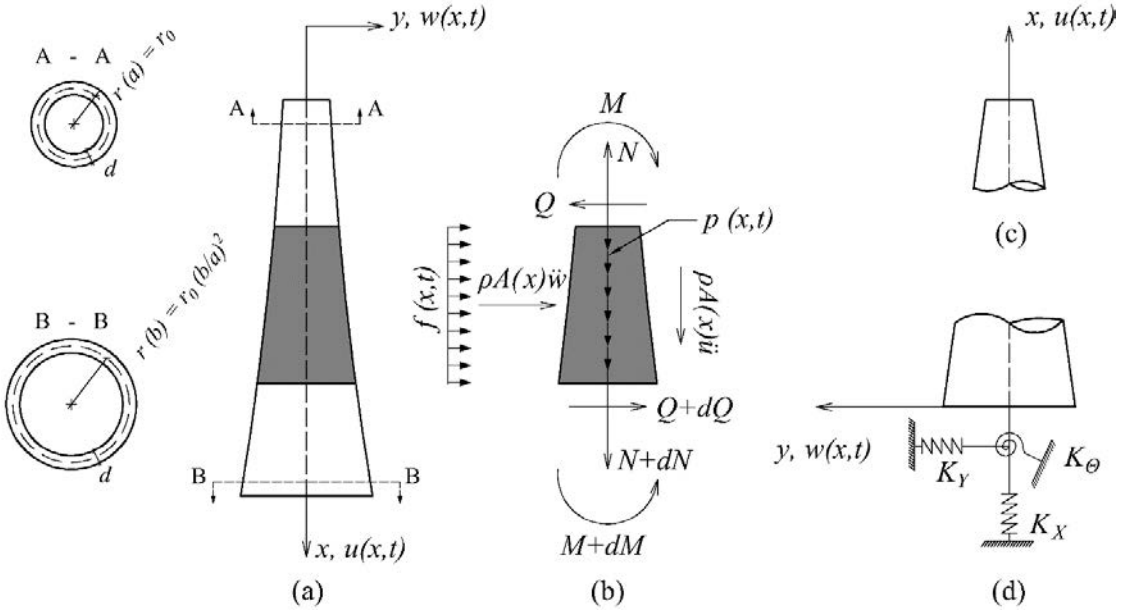

Figure 3: (a) Cantilevered pylon mechanical model with a variable cross-section; (b) free body diagram; (c), (d) top and base conditions

Property and/or dimension	Symbol	Value	Units
Modulus of Elasticity	E	$230 \cdot 10^3$	GPa
Mass density	ρ	7.88	t/m^3
Cross-section mean radius at the top	$r(a)$	84.8	mm
Cross-section mean radius at the base	$r(b)$	103	mm
Cross-section effective thickness	d	2.5	mm
Pylon height	L	2.48	m
Equivalent base springs	K_X	∞	kN/m
	K_Y	∞	kN/m
	K_Θ	4621	kNm/rad

Table 1: Mechanical properties and dimensions of the industrial pylon

A preliminary assessment of the degree of fixity of the pylon showed that the base plate may warp when lateral forces are applied because of its small thickness of 20 mm. A quasi-static experiment was therefore carried out as shown in Fig. 4, whereby a lateral force of $F = 680$ kgf was applied at a height of $L_1 = 2.27$ m, resulting in a total displacement of $u = 22$ mm that was measured slightly below, at a height of $L_2 = 2.22$ m. Since the base plate rotation contributes to this movement, the plate displacement relative to the floor was also measured and was equal to 7.27 mm. Thus, the equivalent rotational spring constant was computed from the following equation:

$$u(x) = \left(\frac{1}{E}\right)\int_0^x (1/I(x))\{M_{,P}(x)M_{,1}(x)\}\,dx + \{M_{,P}(L_1)\cdot M_{,1}(L_1)\}/K_\Theta = 14.73 + 7.27 = 22 \text{ mm} \quad (1)$$

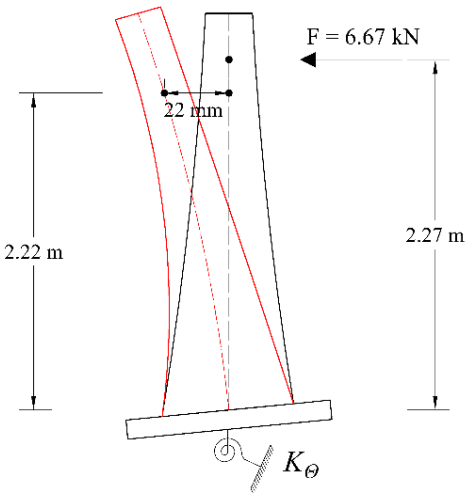

Figure 4: Lateral force applied quasi-statically to the pylon for evaluating the degree of base fixity

The spring constant was found to be equal to $K_\theta = 4621$ kNm/rad. In the above, $M(x)$ are the moment diagrams that develop in the cantilevered, tapered pylon because of the load at $x = L_1$ plus a unit force at $x = L_2$.

3 MECHANICAL MODEL

The governing equations of motion for the tapered, cantilevered beam with distributed mass shown in Fig. 3 derive from the equilibrium diagram of a differential segment dx under distributed longitudinal $p(x,t)$ and transverse $f(x,t)$ loads [25]

$$\frac{\partial}{\partial x}\left(EA(x)\frac{\partial u(x,t)}{\partial x}\right) - m(x)\frac{\partial^2 u(x,t)}{\partial t^2} = p(x,t) \tag{2}$$

$$\frac{\partial^2}{\partial x^2}\left(EI(x)\frac{\partial^2 w(x,t)}{\partial x^2}\right) + m(x)\frac{\partial^2 w(x,t)}{\partial t^2} = f(x,t) \tag{3}$$

where $u(x,t)$, $w(x,t)$ are the longitudinal and transverse displacements. Also, $EA(x)$ and $EI(x)$ are the variable axial and bending stiffness of the pylon, $m(x)$ is its mass per unit length and $L = b - a$ is the height. Next, the axial force, bending moment, and shear force are defined as $N = EA(x)(\partial u/\partial x)$, $M = -EI(x)(\partial w^2/\partial x^2)$, $Q = -EI(x)(\partial w^3/\partial x^3)$. Initial conditions are zero and the boundary conditions for the fixed-base case are:

$$M(a,t) = Q(a,t) = N(a,t) = 0 \text{ and } w(b,t) = \partial w(b,t)/\partial x = u(b,t) = 0 \tag{4}$$

By differentiating the variable stiffness terms, the equations of motion become

$$EA(x)u'' + [EA(x)]'u' - m(x)\ddot{u} = p(x,t) \tag{5}$$

$$EI(x)w'''' + 2[EI(x)]'w''' + [EI(x)]''w'' + m(x)\ddot{w} = f(x,t) \tag{6}$$

Note that for viscoelastic material behavior, the modulus of elasticity becomes a complex number $\hat{E} = E(1 + i\delta)$, where δ is the dimensionless damping coefficient. The notation introduced above uses primes ($'$) and dots ($\cdot$) to respectively denote differentiation with respect to spatial coordinate *x* and time *t*.

If complete base fixity cannot be assumed, the boundary conditions change to

$$M(a,t) = Q(a,t) = N(a,t) = 0 \quad \text{and}$$
$$M(b,t) = -K_\Theta \dot{w}(b,t), Q(b,t) = -K_Y w(b,t), N(b,t) = -K_X u(b,t) \tag{7}$$

The consequence is that constants which appear in the analytical solutions for the fixed base have to be re-evaluated for these new boundary conditions.

4 EXPERIMENTAL SETUP

The first industrial pylon was placed in the Laboratory for cyclic testing and the basic setup was shown in Fig. 1. Specifically, a steel collar was placed at the top and the base was bolted to a steel plate, which in turn was bolted through use of steel angles to the strong floor. An actuator was then attached to the adjacent strong frame to provide lateral forces and was placed at the same height as the steel collar, with a steel rod used to connect the actuator piston to the collar.

4.1 Cyclic testing for pylon fatigue

In the first round of cyclic testing for fatigue, the actuator provided a lateral force to the top of the cantilevered pylon, which was supported at the base by four pre-stressed steel anchors. Details are shown in Fig. 5, with the lateral force applied at a distance 2270 mm from base via a Schenck dynamic actuator with a maximum load capacity of 250 kN. The actuator was equipped with an MTS load cell with a maximum capacity of 50 kN for recording the applied force during the experimental procedure. At roughly the same location (2180 mm) as the applied force, a linear variable differential transducer (LVDT) displacement transducer (labelled as $K10$) was placed to measure the horizontal displacement of the pylon. Two additional displacement transducers (labelled as $S4$ and $M1$) were used for measuring the vertical displacement at the bottom of the column and at each face, in an effort to calculate the rotation of the base cross-section, as was discussed in Section 2. The pylon was subjected to cyclic loading by using a controlled horizontal force, with a maximum magnitude of ± 5 kN and at a frequency of 3 Hz for a total of 80,000 cycles. The experimental procedure lasted for about seven and a half hours, after which the pylon was visually inspected to detect possible cracks and weld failures. Hairline cracks were observed at the base area, which indicates the onset of damage and necessitates the use of remedial measures.

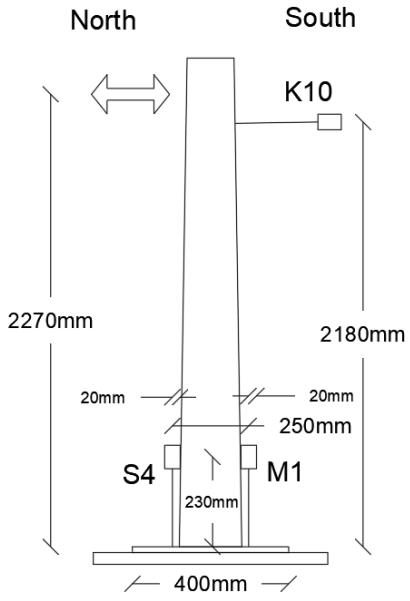

Figure 5: Experimental setup for fatigue testing of the industrial pylon

4.2 Impact hammer measurements

Before and after the aforementioned fatigue test, impact hammer tests were carried out to determine the dynamic properties of the pylon and to identify any changes due to structural deterioration. The pylon was struck with a series of impact hammer blows at about mid-height and three accelerometers placed at the top, mid-height and base of the pylon measured the resulting acceleration time histories. The G-Link-200 type accelerometers, provided by the Lord-Microstrain Sensing Systems company, were used and data was collected in a WSDA-2000 Aggregator unit with wireless transmission to a PC for storage and processing. Following an FFT of the time histories, the eigenvalues were directly measured from the frequency plots. Furthermore, use of OMA produces a matrix that is subsequently processed by the Frequency Domain Decomposition (FDD) technique for the recovery of the eigenvectors [26]. No measurable changes in the first three eigenproperties (i.e., natural frequencies and modal shapes) of the pylon were observed between the first batch of measurements prior to fatigue testing and the follow-up batch of measurements conducted after the pylon had been tested, despite the presence of the hairline base cracks in the latter case. However, a diffusion around the peaks in the Fourier transform of the displacements at the three measuring stations was observed, indicating the presence of equivalent material damping effects.

4.3 DIC system implementation

In an effort to recover a more complete picture of the deformations of the pylon during the onset of the loading cycles, a DIC system was set up facing the second industrial pylon, which was intact, see Fig. 6. This setup is tailored for registering two-dimensional fields for in-plane displacements. It comprises a camera connected and controlled by a computer, plus light sources [27]. The lens of a Sony A6000 camera focused on the central vertical line along the pylon's front side and consecutive frames were captured every 2 s. The camera CCD matrix size is $23.5x15.6$ mm, which provides an image resolution of $6000\ x\ 4000$ pixels, with a pixel size of approximately 3.9 μm. Five reversible loading cycles were applied to the pylon by the actuator, as shown in Fig. 6. During one such experiment, 150 images of the studied object were registered. After completion of the experiment, all captured images were processed using software written in C^{++} language and running in an MS Windows environment. Following the DIC method, the first of the registered images is use as reference. The images were processed using a correlation subset of 32×32 size grid with a 32 pixels. This way, a smooth surface with a measured point density of about 15 mm was achieved. In the current experiments, the most important data concerns the middle vertical line of the pylon, although here we will focus on the top point of this line.

As mentioned previously, the DIC implemented here is based on a comparison of simulated random patterns, generated according to a new algorithm [27]. A criterion for the quantitative evaluation of the random patterns is established following the calculation of their autocorrelation functions. These deformation patterns are realized both experimentally and simulated numerically from the data. The random patterns retain good quality until an increase of 20% in their deformation level is reached. The speckle-image is directly stored in the computer memory at discrete, equidistant time steps, thus allowing

the tracking process to evolve and yield a time sequence of the deformation field that develops in the tested pylon.

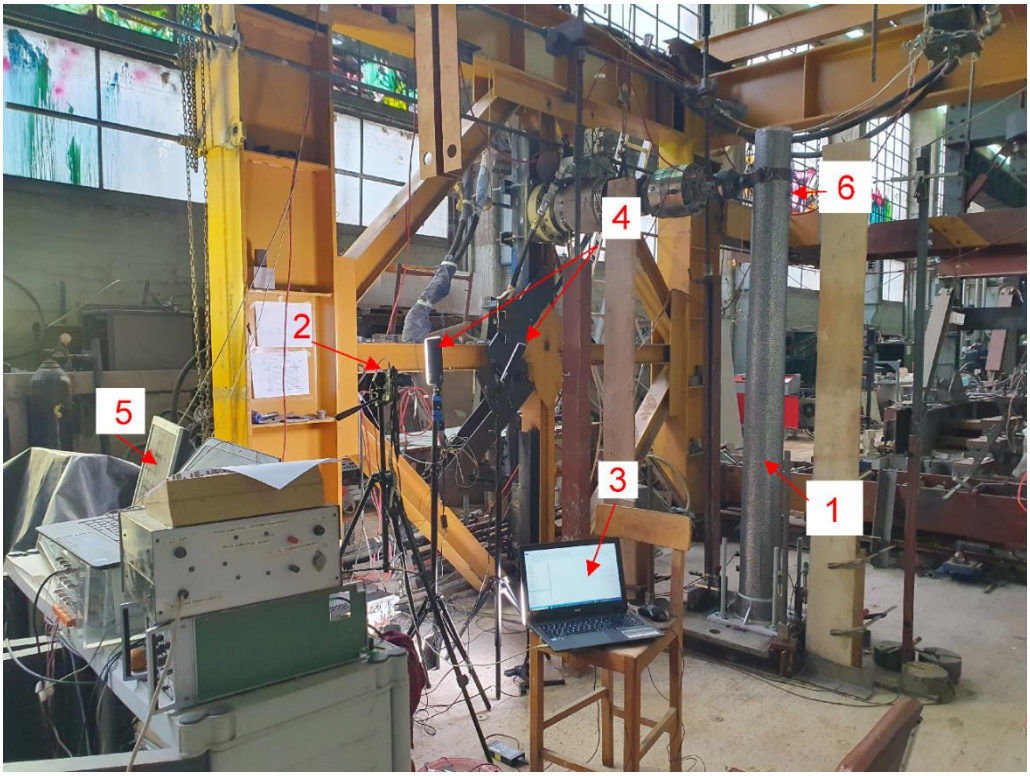

Figure 6: DIC setup for the industrial pylon. Legend: 1- pylon; 2- camera; 3 – laptop computer; 4 - lighting fixtures; 5 - displacement measuring unit; 6 – Actuator and LVDT

5 ANALYTICAL SOLUTIONS

The governing equations of dynamic equilibrium are solved for both axial and flexural vibrations, but only final results are given here, as the solution procedure has been elaborated elsewhere [28].

5.1 Axial vibrations

For a harmonic base motion $u_g(t) = u_{go}e^{i\Omega t}$, the forcing function in the vertical direction is $p(x,t) = -m(x)\ddot{u}_g(t) = m(x)\Omega^2 u_{go}e^{i\Omega t}$. The axial displacement is a complex variable, i.e., $u(x,t) = u_o(x)e^{i\Omega t}$, and the amplitude is written in terms of its absolute value as $u_o(x) = |u_o(x)|\, e^{i\theta}$, with θ the phase angle. Examining the reference case of a uniform pylon with a cross-section radius that at the top, $r = r(a)$, the equation of motion simplifies to

$$u_o'' + \hat{z}^2 u_o = -\hat{z}^2\, u_{go}, \quad \hat{z} = C_P^{-1}\sqrt{1/(1+i\delta)}\,\Omega \tag{8}$$

where $C_P = \sqrt{\hat{E}/\rho}$ is the P-wave velocity and ρ the mass density. The homogenous boundary conditions at the base and top, $u_0(b) = 0$ and $\hat{E}A\, u_0'(a) = 0$, are now used to recover the constants in the solution $u_0(x) = c_1 \cos \hat{z}x + c_2 sin\ \hat{z}x - u_{go}$. The ratio of top to bottom displacements, $U_0 = u_0(x = a)/u_{g0}$, is independent of the input and plays the role of a dimensionless, complex-valued transfer function:

$$U_0(\Omega) = sec\hat{z}L - 1 = |U_0(\Omega)|e^{\,i\,\theta_0(\Omega)} \tag{9}$$

Next, the equation of motion for the non-uniform cantilevered pylon that displays a quadratic variation of its cross-section area with height is $A(x) = A_o(x/\alpha)^2, a \le x \le b$, and under harmonic ground motion derives from Eq. (5):

$$x^2\ u_o''\ +\ 2x\, u_o' + \hat{z}^2\, x^2\, u_o = -\hat{z}^2 x^2\, x_{go} \tag{10}$$

The above is a Bessel equation with the solution $u_0(x) = x^{-1/2}(c_1\, J_{1/2}(\hat{z}x) + c_2 J_{-1/2}(\hat{z}x)) - u_{go}$, where J_n are Bessel functions of the first kind and fractional order n. Imposition of the boundary conditions for a fixed base yields the following normalized transfer function:

$$\frac{U_0(\Omega)}{} = -1 + \frac{b}{a}\frac{\{\hat{z}\mathrm{a}\cos(\hat{z}a) - \sin(\hat{z}a)\}\cos(\hat{z}a) - \{-\hat{z}\mathrm{a}\sin(\hat{z}a) - \cos(\hat{z}a)\}\sin(\hat{z}a)}{\{\hat{z}\mathrm{a}\cos(\hat{z}a) - \sin(\hat{z}a)\}\cos(\hat{z}b) - \{-\hat{z}\mathrm{a}\sin(\hat{z}a) - \cos(\hat{z}a)\}\sin(\hat{z}b)} \tag{11}$$

5.2 Flexural vibrations

The forcing function here also derives from base motion, but in the horizontal direction, namely $f(x,t) = -m(x)\ddot{x}_g(t) = m(x)\Omega^2 w_{go} e^{i\Omega t}$. Starting with a uniform pylon, the governing equation is an ordinary differential equation of the fourth order with a frequency-dependent coefficient $\hat{z}$:

$$w_o'''' - \hat{z}^4 w_o = \hat{z}^4\, w_{go},\ \ \hat{z}^4 = \rho A\Omega^2/EI(1 + i\delta) \tag{12}$$

The transverse displacement is $w(x,t) = w_o(x)e^{i\Omega t}$, with the amplitude $w_o(x) = |w_o(x)|\, e^{i\theta}$. The solution to the above equation is $w_0(x) = c_1 \sinh \hat{z}x + c_2 \cosh \hat{z}x + c_3 \sin \hat{z}x + c_4 \cos \hat{z}x - w_{go}$. By imposing the boundary condition, namely $w_0(b) = 0, w_0'(b,t) = 0$ at the base and $w_0'''(a) = 0, EI\, w_0''(a) = 0$ at the top, allows for the evaluation of the constants appearing in this solution. The dimensionless transfer function for flexural vibrations is defined as $W_0 = w_0(x = L)/w_{go}$, yielding

$$W_0(\Omega) = (c_1 \sinh \hat{z}L + c_2 \cosh \hat{z}L + c_3 \sin \hat{z}L + c_4 \cos \hat{z}L) - 1, \text{ where}$$

$$c_1 = \frac{-\cosh \hat{z}L\ \sin \hat{z}L - \sinh \hat{z}L\ \cos \hat{z}L}{2 + 2\cosh \hat{z}L \cos \hat{z}L} \tag{13}$$

$$c_2 = \frac{\sinh \hat{z}L \ \sin \hat{z}L + \cosh \hat{z}L \ \cos \hat{z}L + 1}{2 + 2 \cosh \hat{z}L \cos \hat{z}L}$$

$$c_3 = \frac{cosh \, \hat{z}L \ \ sin \, \hat{z}L + sinh \, \hat{z}L \ \ cos \, \hat{z}L}{2 + 2 \cosh \hat{z}L \cos \hat{z}L}$$

$$c_4 = \frac{1 - sinh \, \hat{z}L \ \ sin \, \hat{z}L + cosh \, \hat{z}L \ \ cos \, \hat{z}L}{2 + 2 \cosh \hat{z}L \cos \hat{z}L}$$

Next, the tapered pylon with a variable cross-section radius r that results in a quadratic cross-section area and a sixtic moment of inertia, $A(x) = A_o(x/a)^2, I(x) = I_o(x/a)^6$. By introducing a dimensionless variable $\xi = x/a$, where $1 \le \xi \le (b/a)$, Eq. (6) reads as:

$$\xi^4 \, w_o''''(\xi) + 12 \, \xi^3 \, w_o'''(\xi) + 30 \, \xi^2 \ + w_o''(\xi) - \hat{z}^4 \ w_o(\xi) = \hat{z}^4 \ w_{go} \tag{14}$$

with parameter $\hat{z}^4 = \rho A_o \Omega^2 a^4 / \hat{E} I_o$. The solution to this fourth-order Euler equation is

$$w_o(\xi) = c_1 A_1(\xi) + c_2 A_2(\xi) + c_3 A_3(\xi) + c_4 A_4(\xi) - w_{go} =$$
$$= c_1 \, \xi^{-\frac{3}{2} + \frac{\sqrt{\hat{k}+17}}{2}} + \ c_2 \, \xi^{-\frac{3}{2} - \frac{\sqrt{\hat{k}+17}}{2}} + c_3 \ \xi^{-\frac{3}{2}} \sin\left(\frac{\sqrt{\hat{k}-17}}{2} \ln \xi\right) + c_4 \ \xi^{-\frac{3}{2}} \cos\left(\frac{\sqrt{\hat{k}-17}}{2} \ln \xi\right) - w_{go} \tag{15}$$

where $\hat{k} = 4\sqrt{\hat{z}^4 + 4}$ is a parameter. Imposition of the boundary conditions results in the following system of equations for the recovery of values for the constants $c_1 - c_4$:

$$\begin{bmatrix} A_1(b/a) & A_2(b/a) & A_3(b/a) & A_4(b/a) \\ A_1'(b/a) & A_2'(b/a) & A_3'(b/a) & A_4'(b/a) \\ A_1''(1) & A_2''(1) & A_3''(1) & A_4''(1) \\ A_1'''(1) & A_1'''(1) & A_3'''(1) & A_4'''(1) \end{bmatrix} \cdot \begin{Bmatrix} c_1 \\ c_2 \\ c_3 \\ c_4 \end{Bmatrix} = \begin{Bmatrix} w_{go} \\ 0 \\ 0 \\ 0 \end{Bmatrix} \tag{16}$$

In the above, the derivatives of $A(\xi)$ are with respect to the dimensionless spatial variable ξ. It is not necessary to explicitly solve the above system but compute these constants by numerical inversion for every value of the frequency spectrum and substitute in Eq. (15). The solution at the top of the pylon, where $\xi = 1.0$, simplifies because $A_1(1) = A_2(1) = A_4(1) = 1, A_3(1) = 0$. Therefore, the transfer function is now

$$W_0(\Omega) = \ (1/x_{go}) \cdot (c_1 + c_2 + c_4) - \ 1 \tag{17}$$

6 FINITE ELEMENT MODELLING

The FEM software program ANSA [29] was used to model the industrial pylon and a detailed discretization scheme was implemented. Specifically, shell finite elements were employed, with each shell element having 4 nodes and 6 DOF per node. A total of 20 shell elements per cross section, equally spaced in the radial direction, were used. Furthermore, 100 such cross-sections, also equally spaced, were repeated along the height of the pylon yielding a total of 4,000 nodes and resulting in 24,000 DOF. Of course, this type of FEM

model reproduces additional modes of vibration, such as torsional and 'breathing' modes, which are absent if the induced vibrations are of the flexural type. As far as modelling details go, the connection to the base of the pylon did not produce full fixity, so that the base plate and supporting angles were also modelled, along with the four bolts connecting them to the floor. The bolts were modelled by two unyielding springs in the vertical and horizontal directions (K_x, K_y), see Table 1. These modelling details were necessary since they influence the pylon's eigenproperties, even in the low frequency range, something that was confirmed by the results produced by the analytical model of Section 5.

The equation of motion of the pylon modeled as a multi-DOF system under external loads has the general form outlined below

$$\mathbf{M}\ddot{\mathbf{u}}(t) + \mathbf{C}\dot{\mathbf{u}}(t) + \mathbf{K}\mathbf{u}(t) = \mathbf{F}(t) \tag{18}$$

where **M, C, K, F** respectively are the mass, damping and stiffness matrices, and the external force vector. Initial conditions on the displacement and velocity vectors $\mathbf{u}(t=0), \dot{\mathbf{u}}(t=0)$ must also be assigned in conjunction with Eq. (18). Next, Rayleigh's method is used to construct the damping matrix as a linear combination of the mass and stiffness matrices, with the two constants required in this representation evaluated by matching a damping ratio of $\zeta = 5$ (%) assigned to the first two modes of vibration. Finally the natural frequencies ω_i (rad/s) and associated modal shapes φ_i , where $i = 1,2,\ldots,N$ with N the total number of active DOF, are computed from the free vibration problem $\mathbf{K} - \omega^2\mathbf{M} = 0$, with the determinant of this matrix system yielding the characteristic polynomial.

7 DYNAMIC TESTING RESULTS

At first, Table 2 lists the three first eigenfrequencies for axial and flexural vibrations of the steel pylon, as computed from the analytical solutions in Section 5. All computations were carried out using the Python [30] software package. The indication 'homogeneous pylon' refers to an equivalent pylon of constant cross-section with a mean radius being the average value between top and bottom, i.e., $r = 93.9$ mm. Since tapering of the industrial pylon is mild, the eigenfrequencies are close in value. As expected, the flexural eigenfrequencies are much lower in numerical value as compared to the axial ones. Furthermore, the absence of complete fixity in the base clearly influences the flexural eigenfrequencies, showing a deviation of 21% for the first (dominant) eigenfrequency, which decreases to 16% and 13% for the next two higher eigenfrequencies.

Eigenfrequency	$n = 1$	$n = 2$	$n = 3$
Axial vibrations, homogeneous pylon	544.57	1633.7	2722.8
Axial vibrations, tapered pylon	566.28	1641.2	2727.3
Flexural vibrations, homogeneous pylon	32.63	204.46	572.50

Flexural vibrations, tapered pylon	36.57	211.27	577.70
Flexural vibrations, tapered pylon with rotational base spring	28.67	177.54	505.50

Table 2: Sequence of pylon eigenfrequencies f_n (Hz) of the industrial pylon

Next, the first flexural eigenfunction $\varphi_1(\xi)$, which is the dominant contribution to the pylon transverse motions, is recovered from Eq. (15). Coefficients c_i are computed from Eq. (16) by ignoring the base motion contribution ($w_{g0} = 0$), and the following values are obtained: $c_1 = 0.056287, c_2/c_1 = 6.478247, c_3/c_1 = -5.239946, c_4/c_1 = 10.287982$ The eigenfunction is therefore the resulting displacement function $w_0(\xi)$ normalizing by setting the first coefficient equal to unity, i.e., $c_1 = 1$. Figure 7 plots both the analytically obtained eigenfunction, plus the experimentally derived curve using the impact hammer test, from measurements using accelerometers at four equidistant locations along the pylon's height. At the same time, the first eigenfrequency is measured as $f_1 = 27.47$ Hz, a value which is 4% off as compared to the computed eigenfrequency of $f_1 = 28.67$ Hz, see Table 2. In Fig. 7, excellent agreement is observed between the measured and computed eigenfrequencies, with a Modal Assurance Criterion value of $MAC = 0.99996$. Note that this criterion is computed as $MAC = (\varphi_E \cdot \varphi_A^T)^2/\{(\varphi_E \cdot \varphi_E^T) \cdot (\varphi_A \cdot \varphi_A^T)\}$, where subscripts A, E stand for 'analytical' and 'experimental' quantities and superscript T is the transpose operator.

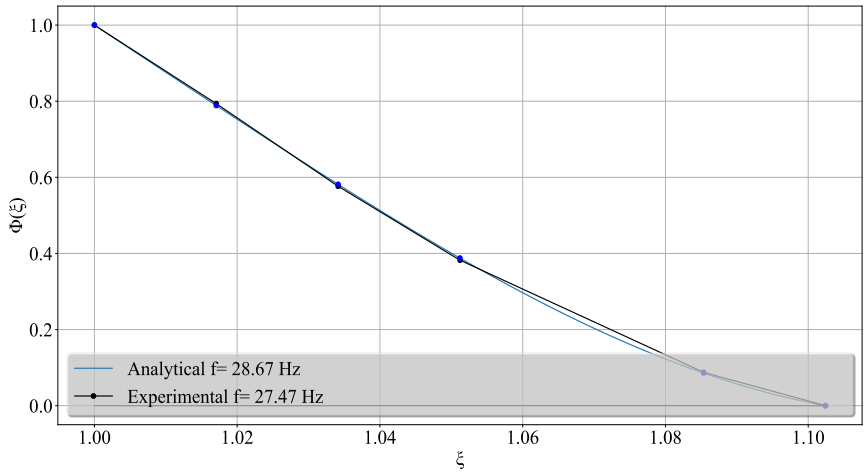

Figure 7: Comparison between the analytically computed and experimentally measured first flexural eigenfunction φ_1 of the tapered pylon versus normalized pylon height ξ

The next series of results are generated from the FEM model described in Section 6 using shell finite elements. These are given in Fig. 8, which depicts the FEM mesh with the first and second modal shapes (i.e., the eigenvectors), which are both of the flexural type. The corresponding eigenfrequencies are f_1 = 28.58 Hz and f_2 = 161.80 Hz. Furthermore, the quasi-static displacement and strain distributions in the pylon are also

shown that resulted from a slowly increasing force applied by the actuator and reaching a value of 0.6 tn.

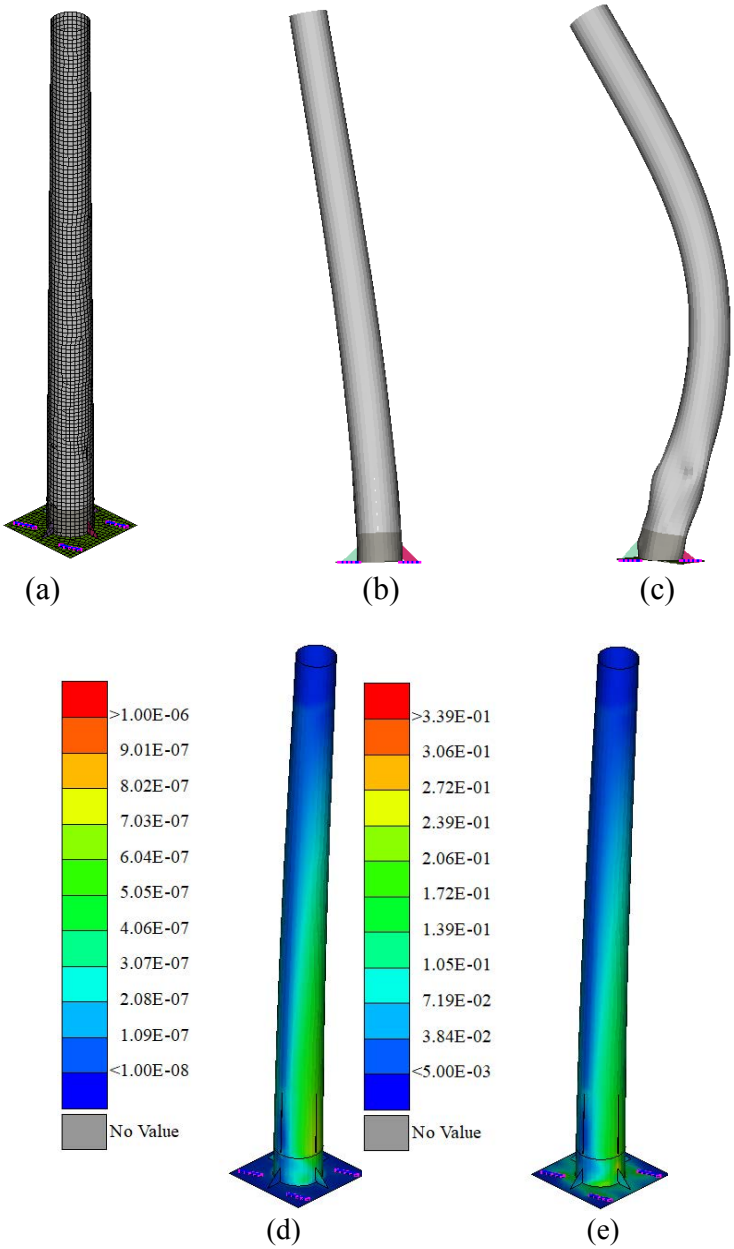

Figure 8: FEM analysis of the industrial pylon: (a) mesh produced using shell elements and including base modelling details, (b) the first mode shape, (c) the second mode shape, (d) the quasi-static deformed shape of the pylon and (e) the associated strain field

We note here the nearly complete agreement between the analytical, the FEM and the experimental-analytical results. It is noted here that the analytical model previously discussed is extremely efficient in terms of savings in computational resources as compared to the FEM. Otherwise, execution times are minimal, i.e., are in the order of a few ms.

8 CYCLIC TESTING RESULTS

Two cyclic load tests were first run on the second (replacement) intact industrial pylon following the first series of fatigue tests, using the DIC setup as is depicted in Fig. 6. In the first test, the actuator at the top was programmed to produce a slowly varying, sinusoidal load reaching a peak force of 0.6 tn and lasting 300 s, as shown in Fig. 9(a). At the same time, Fig. 9(b) plots the top horizontal displacement as measured by the DIC system. The second test involved an alternating, quasi-static ramp load of the same magnitude as before, which lasted 150 s, see Fig. 10(a), while Fig. 10(b) shows the resulting top displacement. Finally, a third test was run with the slowly varying sinusoidal load set at a lower magnitude of 0.42 tn and the conventional displacement measurement technique using an LVDT was activated, along with the DIC system. Figure 11 plots the time evolution of the top displacement as recorded and processed by both methods, where excellent agreement can be observed.

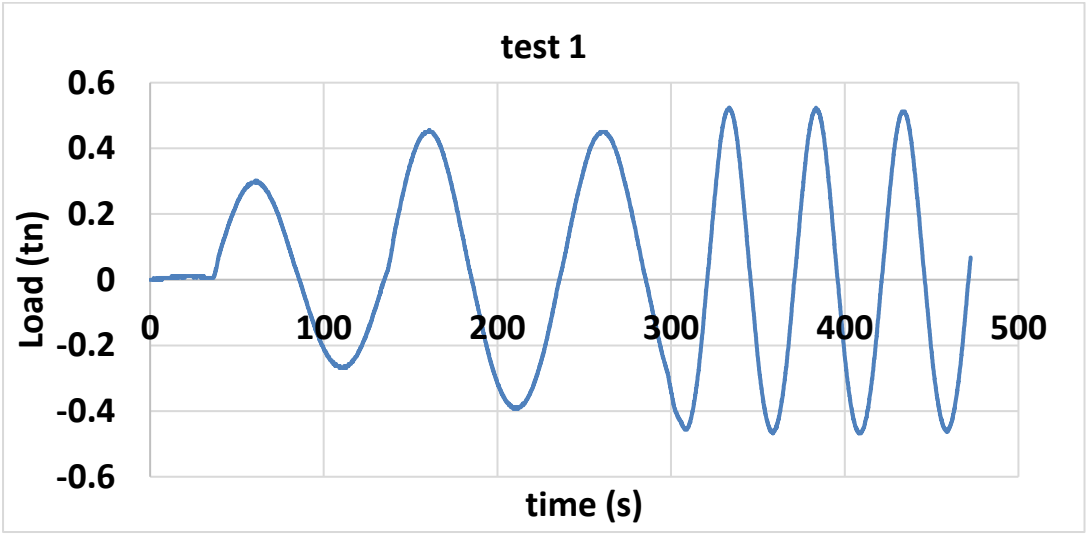

(a)

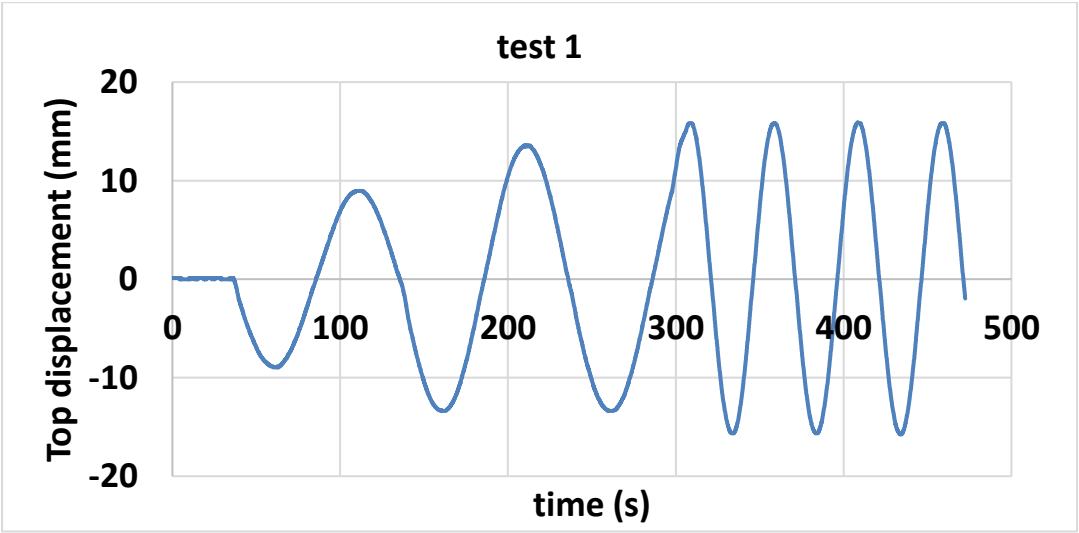

(b)

Figure 9: Cyclic testing using a slowly varying sinusoidal load with the DIC data recording and processing system: (a) Applied force and (b) resulting transverse displacement, both measured at the top of the pylon

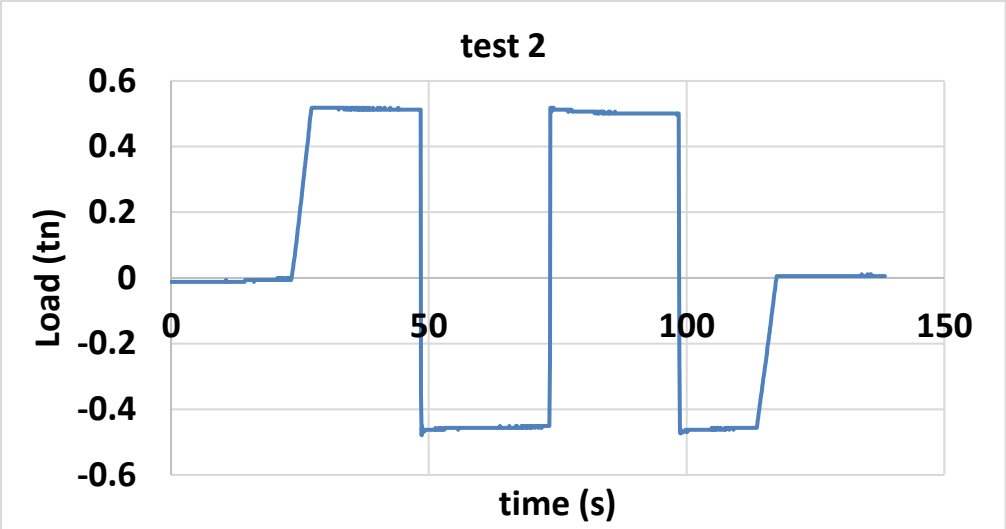

(a)

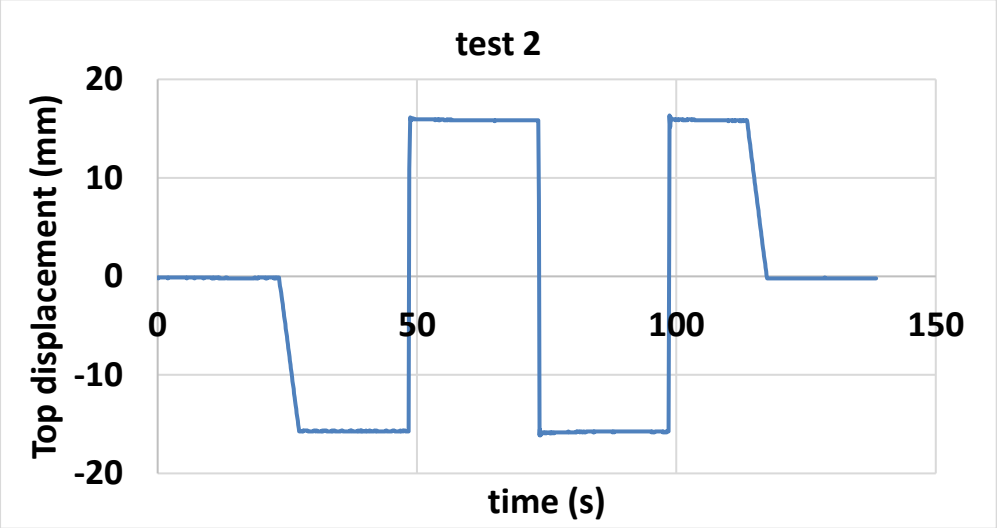

(b)

Figure 10: Cyclic testing using a quasi-static ramp load with the DIC data recording and processing system: (a) Applied force and (b) resulting transverse displacement, both measured at the top of the pylon

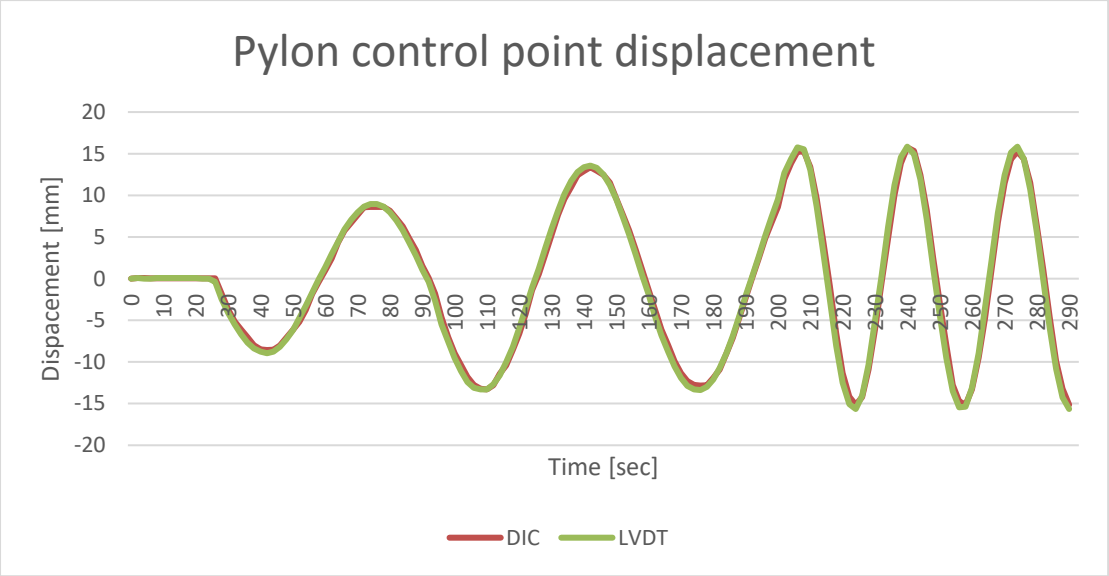

Figure 11: Cyclic testing using a slowly varying sinusoidal load showing the top displacement as recorded by both the DIC system and the LVDT apparatus

9 DISCUSSION AND CONCLUSIONS

Pylons are ubiquitous, serving as supports for power lines, for telecommunication equipment, for lighting devices, for wind turbines, etc. As such, certification of their performance is important, since they are invariably mass-produced and their specifications are tailored to satisfy code-prescribed design requirements. In this work, two $2.5\,m$ metallic, circular cylindrical cantilevered pylons with a variable, ring-type cross-section for providing long-term highway illumination were examined. An important design consideration is fatigue, as these pylons are exposed year-round to wind pressure. Corrosion resistance is addressed by a zinc coating of the external surface, which provides negligible additional strength to the pylon. Fatigue testing completed here has shown that after 80,000 cycles of cyclic, low frequency, low amplitude loading the pylon developed hairline cracks at its base, whose presence cannot be detected by impact hammer of similar dynamic tests. These cracks, however, act as stress concentrators with the potential for compromising the structural integrity of the pylon. More specifically, the impact hammer tests which followed before and after the cyclic testing, showed no measurable change in the dynamic properties of the cantilevered pylon. Next, a DIC system was implemented on the second (intact) pylon as a means for capturing the development of the kinematic field from a series of time frames depicting the displacement evolution over the front surface of the pylon, which because of load symmetry is the same as that developing in the back surface. These preliminary DIC studies, conducted for cyclic loads, were in excellent agreement with the conventional method of tracing the displacement vector at a fixed location on the pylon. The next stage in the future is to reproduce the strain fields at the base of the pylon as the cracks begin to appear, which would give a good picture of crack growth. Overall, we note the good agreement of the experimentally obtained results with the analytical / numerical predictions for this experimental investigation.

The basic findings documented in this work are deemed useful in developing SHM protocols in engineering practice to help with the structural identification of pylon integrity, especially since a large number of pylons comprise a functional network. These protocols could include a simple monitoring system placed at critical locations of a few representative pylons, supplemented with a wireless transmission system sending data to a central unit. This data, after an initial evaluation regarding its importance, could be compared against benchmarks to conclude if the pylon is in distress and needs to be inspected for a better assessment of its functionality.

Acknowledgements: The authors acknowledge support from the German Research Foundation (DFG) under grant SM 281/20-1 and the Hellenic Foundation for Research and Innovation (HFRI) for providing Fellowship No. 6522. Dipl. Ing. Kosmas Dragos, Technical University of Hamburg-Harburg, is acknowledged for providing the FEM solutions.

REFERENCES

[1] B.R Ellingwood, D.J. Naus. Condition assessment and maintenance of aging structures in critical facilities, a probabilistic approach. D. M. Frangopol, ed., *Case Studies in Optimal Design and Maintenance Planning of Civil Infrastructure Systems*, ASCE Structural Engineering Institute Publication, Reston, 1999.

[2] T.D. O'Rourke. Critical infrastructure, interdependencies and resilience. *The Bridge,* **37**(1), 22–29, 2007.

[3] J.P. Lynch, K.J. Loh. A summary review of wireless sensors and sensor networks for structural health monitoring. *The Shock and Vibration Digest*, **38**(2), 91-128, 2006.

[4] C.R. Farrar CR, K. Worden K. *Structural Health Monitoring: A Machine Learning Perspective.* Wiley, Chichester, 2012

[5] D.E. Adams. *Health Monitoring of Structural Materials and Components: Methods with Applications*. Wiley, Hoboken, 2007.

[6] K. Smarsly, K.H. Law. A migration-based approach towards resource-efficient wireless structural health monitoring. *Advanced Engineering Informatics*, **27**(4), 625–635, 2013.

[7] S. Sony, S. Laventure, A. Sadhu A. A literature review of next-generation smart sensing technology in structural health monitoring. *Structural Control and Health Monitoring*, **26**: e2321. doi:10.1002/stc.2321, 2019.

[8] E. Kausel *Advanced Structural Dynamics*, Cambridge University Press, Cambridge, 2017.

[9] C.W.S. To. Vibration of a cantilever beam with base excitation and tip mass. *Journal of Sound and Vibration*, **83**(4), 445–460, 1982.

[10] M. Gurgoze. A note on the vibrations of restrained beams and rods with point masses. *Journal of Sound and Vibration*, **96**(4), 461–468, 1983.

[11] V. Zania. Natural vibration frequency and damping of slender structures founded on monopoles. *Soil Dynamics and Earthquake Engineering*, **59,** 8–20, 2014. doi: 10.1016/j.soildyn.2014.01.007

[12] J. Freundlich. Transient vibrations of a fractional Kelvin-Voigt viscoelastic cantilever beam with a tip mass and subjected to base excitation. *Journal of Sound and Vibration*, **438**, 99–115, 2019.
[13] G.D. Manolis, P.K. Koliopoulos. *Stochastic Structural Dynamics in Earthquake Engineering.* WIT Press, Southampton, 2001.
[14] T.T. Soong, M.C. Constantinou. *Passive and Active Structural Control in Civil Engineering*, *Series Vol. 345.* CISM International Center for Mechanical Sciences, Springer-Verlag, Vienna, 1994.
[15] C.Y. Chu, T.T. Soong, A.M. Reinhorn. *Active, Hybrid and Semi-Active Structural Control: A Design and Implementation Handbook.* Wiley, Hoboken, 2005.
[16] J. Schijve, *Fatigue of Structures and Materials, 2nd Edition*. Springer, Berlin, 2008.
[17] J. Slavic, M. Boltezar, M. Mrsnik, M. Cesnik, J. Javh, *Vibration Fatigue by Spectral Methods: From Structural Dynamics to Fatigue Damage.* Elsevier, Amsterdam, 2020.
[18] K. Smarsly, K.H. Law, D. Hartmann. Towards life-cycle Management of wind turbines based on structural health monitoring. *Proceedings of the First International Conference on Performance-Based Life-Cycle Structural Engineering*, Hong Kong, 12 May 2012.
[19] B. Peeters. System identification and damage detection in civil engineering structures. *PhD Dissertation*, KU Leuven, Belgium, 2000.
[20] K. Dragos, K. Smarsly. Distributed adaptive diagnosis of sensor faults using structural response data. *Smart Materials and Structures*, **25**(10), 105019, 2016.
[21] L. Zhang, R. Brincker, P. Andersen. An overview of operational modal analysis: Major development and issues. *Proceedings of the 1st International Operational Modal Analysis Conference*, Copenhagen, Denmark, 26 April 2005.
[22] J. Burch, J. Tokarski. Production of multiple beam fringes from photographic scatters, *Optica Acta*, **15**, 101-112, 1968.
[23] W.H. Peters, W. F. Ranson. Digital image techniques in experimental stress analysis. *Optical Engineering*, **21**, 427–431, 1982.
[24] G. Stoilov, V. Kavardzhikov, D. Pashkouleva. Comparative study of random patterns for digital image correlation, *Journal of Theoretical and Applied Mechanics*, **42**(2), 55–66, 2012.
[25] S.S. Rao. *Vibration of Continuous Systems.* Wiley, Hoboken, 2007.
[26] K. Dragos, T. Makarios, I. Karetsou, G.D. Manolis, K. Smarsly, Detection and correction of synchronization-induced errors in operational modal analysis. *Archive of Applied Mechanics*, **90**, 1547-1567, 2020. doi: 10.1007/s00419-020-01683-6
[27] G. Stoilov, V. Kavardzhikov. Application of digital image correlation method to solid mechanics. *Proceedings of the 12th National Congress on Theoretical and Applied Mechanics*, Varna, Bulgaria, 23-26 September 2013.
[28] G.D. Manolis, G.I. Dadoulis, S.I. Pardalopoulos, K. Dragos. Analytical models for monitoring of flexible antennas under environmentally induced dynamic loads. *Acta Mechanica*, **231,** 3621–3624, 2020. doi: 10.1007/s00707-020-02712-9
[29] *BETA CAE Systems, EPILYSIS Finite Element Method Solver*, Thesssaloniki, Greece, 2022. www.beta-cae.com
[30] *Python Software Foundation*, Beaverton, Oregon, 2001. www.python.org